coatings

MDPI

Article

Increased Electromagnetic Wave Absorption through Controlled Sonication Processing on $BaFe_{11.2}Mg_{0.4}Al_{0.4}O_{19}$ Nanoparticles

Erlina Yustanti [1,2,*], Alfian Noviyanto [3,4], Laila Chusnul Chotimah [1], Muhamad Abdur Rais Saputra [1], Maulana Randa [5] and Maykel Manawan [6]

[1] Department of Metallurgical Engineering, Faculty of Engineering, Sultan Ageng Tirtayasa University, Jl. Jend. Sudirman KM. 03, Cilegon 42435, Banten, Indonesia
[2] Centre of Excellence, Nanomaterial and Process Technology Laboratory, Faculty of Engineering, Sultan Ageng Tirtayasa University, Jl. Jend. Sudirman KM. 03, Cilegon 42435, Banten, Indonesia
[3] Advanced Materials Research Group, Nano Center Indonesia, Jl. PUSPIPTEK, Tangerang Selatan 15314, Banten, Indonesia
[4] Department of Mechanical Engineering, Mercu Buana University, Jl. Meruya Selatan, Kebun Jeruk 11650, Jakarta, Indonesia
[5] Research and Development Agency, Indonesia Ministry of Defense, Jl. Jati No.1, Pondok Labu 12450, Jakarta, Indonesia
[6] Teknologi Daya Gerak, Fakultas Teknologi Pertahanan, Universitas Pertahanan RI. Kawasan IPSC Sentul, Sukahati, Kec. Citeureup, Kabupaten Bogor 16810, Jawa Barat, Indonesia
* Correspondence: erlina.yustanti@untirta.ac.id; Tel.: +62-0254-395502

Abstract: Electromagnetic waves show rapid development in electronics, telecommunications, and the military. One of the efforts to overcome the effects of electromagnetic interference is by developing microwave-absorbing materials. Barium hexaferrite is the best candidate for development as an absorber material. Microwave absorption in barium hexaferrite can be increased through Mg-Al doping and reducing the particle size. This study aimed to analyze sonication parameters to reduce the particle size by combining destruction methods using mechanical alloying followed by high-power ultrasonic irradiation. Barium hexaferrite was synthesized through mechanical alloying by mixing stoichiometric $BaCO_3$, Fe_2O_3, Al_2O_3, and MgO (Sigma-Aldrich p.a 99%) (Mg-Al 0.4%wt). The samples continued the sintering process at 1200 °C for 2 h to grow crystal embryos. The optimal parameters for ultrasonic destruction were using a transducer:reactor diameter ratio of 1:10, a particle density of 5 g/250 mL, and adding a non-ionic surfactant of 0.01% at an amplitude of 55% and a sonication time of 8 h. These methods resulted in the saturation magnetization of 18.50 emu/g and a coercivity of 0.08 Tesla. The reduction in the particle size of BHF doped with Mg-Al was successfully up to 21 nm, resulting in a reflection loss of up to −40.8697 dB at 11.896 GHz (x-band, 8–12 GHz). The BHF nanoparticles doped with Mg-Al effectively absorbed up to 99.99% electromagnetic waves.

Keywords: barium hexaferrite; ultrasonic irradiation; radar-absorbing material; reflection loss

check for updates

Citation: Yustanti, E.; Noviyanto, A.; Chotimah, L.C.; Saputra, M.A.R.; Randa, M.; Manawan, M. Increased Electromagnetic Wave Absorption through Controlled Sonication Processing on $BaFe_{11.2}Mg_{0.4}Al_{0.4}O_{19}$ Nanoparticles. *Coatings* **2022**, *12*, 1367. https://doi.org/10.3390/coatings12091367

Academic Editor: Yuanlie Yu

Received: 20 August 2022
Accepted: 13 September 2022
Published: 19 September 2022

1. Introduction

Electromagnetic interference (EMI) continues to be a problem for electronic devices, radar, communication systems, and human health. For example, EMI can cause the device's performance to degrade or even be damaged. Furthermore, it can also endanger human health. Therefore, using microwave-absorbing materials is imperative to minimize the electromagnetic reflection caused by EMI [1]. Barium hexaferrite ($BaFe_{12}O_{19}$/BHF) is a ferrite-based magnetic material widely used as a microwave absorber. High magnetization, remanence, coercivity, and electrical resistivity are all advantages of barium hexaferrite [2].

Furthermore, as a permanent magnet, BHF can be used as a microwave-absorbing material by modifying its crystal structure by substituting other ions to replace some of the positions of the Ba/Fe ions, resulting in soft magnets. The cations generally used to replace Ba^{2+}/Fe^{3+} ions are Mn, Al, Mg, Co, Ni, Ti, and Zn [3]. The element and dopant concentration affect the quality and performance of the absorber material. For instance, BHF with Mn-Ti dopants is successfully synthesized using the top-down method with 90% microwave absorption [4]. On the other hand, in the bottom-up approach, BHF with Mg-Al dopants is synthesized in 99.97% microwave absorption with a reflection loss of −36.4 dB at 10.6 GHz [5].

BHF-based absorber material synthesis methods include solid state [6,7], ceramic route [8], hydrothermal [9,10], coprecipitation [3,11,12], sol–gel [13–15], sol–gel and auto-combustion [16–18], sonochemistry [19–21], a combination method including citric acid, sol–gel, auto-combustion, and sonochemistry [22], a combination technique comprising coprecipitation, hydrothermal, sol–gel, and microemulsion [23], carboxylation-induced polyaniline [24], and mechanical alloying combined with ultrasonic irradiation [4]. Among these methods, mechanical alloying is an interesting method with easy implementation and without producing chemical waste. The basic principle of mechanical alloying is making a homogeneous and amorphized material. The mixing of powder materials through the stages of repeated cold welding processes, fractures, and re-welding occurs in a high-energy ball mill. The heat treatment of the cystic embryo at 1200 °C produces a single phase of BHF. The bottom-up synthesis of nanoparticles produces higher microwave absorption than the top-down synthesis. However, the bottom-up synthesis is quite complex, requires high costs, produces acid waste, and is challenging to implement on a large scale. Therefore, ultrasonic irradiation is an attractive option because it has low costs, generates no waste, and can be applied on a large scale. For the sonication process to occur optimally, it is necessary to control the parameters with a comprehensive analysis.

In this study, we investigated the effect of a combination method, namely mechanical alloying followed by ultrasonic irradiation. We aimed to create an absorber material with ~100% absorption that can be used as a coating on fighter aircraft to prevent radar detection in the 8–12 GHz (x-band). Some studied parameters include the ratio diameter transducer to the reactor, the density, the types and concentration of surfactants, the amplitude, and the sonication time on the effectiveness of the particle size reduction. The effects of Mg-Al dopant substitution on BHF and the presence of surfactants in preventing agglomeration were comprehensively analyzed.

2. Materials and Methods

The precursors for this study were $BaCO_3$, Fe_2O_3, MgO, and Al_2O_3, standard research grade from Sigma-Aldrich (Saint Louis, MO, USA), with a purity of 99%. These precursors were mixed in a planetary ball mill to form $BaFe_{11.2}Mg_{0.4}Al_{0.4}O_{19}$. The ball-to-powder ratio, speed, and milling time were 10, 300 rpm, and 20 h, respectively. The vial and the ball were made from stainless steel to prevent powder contamination. Moreover, ethanol was used to enhance the dispersion during the milling process. The milled samples were dried at the temperature of 100 °C for 2 h, followed by sintering at 1200 °C for 2 h, so that the crystal embryos grew to form the desired sample of $BaFe_{11.2}Mg_{0.4}Al_{0.4}O_{19}$. The sintered pellet was ground and re-milled using the same parameters to reduce the particle size of Mg-Al-doped BHF before entering the high-power ultrasonic destruction stage. The Mg-Al-doped BHF sonication was performed using a ½¨ probe Qsonica Sonicator Q500 at 20 kHz frequency (Newtown, CT, USA). The amplitude of ½¨ probe at 100% is approximately 120 µm. The parameters of sonication were the ratio of the transducer diameter (d) to the reactor diameter (D) (d/D = 1:6; 1:8; and 1:10), the particle density (5 g/100 mL; 5 g/150 mL; 5 g/200 m; and 5 g/250 mL), as well as variations in the use of surfactants (anionic; cationic; non-ionic; and amphoteric). The addition of 2 drops of non-ionic surfactants with various concentrations of 0%, 0.01%, 0.1%, and 1% was also analyzed to observe the best parameters for preventing the agglomeration of nanoparticles.

Moreover, the effect of the amplitude and sonification time were also thoroughly investigated in this study. Briefly, 5 g of the sample was dissolved in 250 mL of distilled water, and ultrasonic destruction was carried out with amplitude variations of 35%, 45%, and 55% and variations in sonication time of 0, 2, 4, 6, and 8 h. Table 1 shows the details of the samples and their parameters. Figure 1 summarizes the research design in a schematic illustration.

Table 1. Parameters of the sample treatment process.

Sample	A	R	D	S	SC	ST
Code	**Amplitude**	**Ratio d/D**	**Density**	**Surfactant**	**Surfac. Conc.**	**Sonic. Time**
A	55	1:06	5/250	0	0	6
B	55	1:08	5/250	0	0	6
C	55	1:10	5/250	0	0	6
D	55	1:10	5/200	0	0	6
E	55	1:10	5/150	0	0	6
F	55	1:10	5/100	0	0	6
G	55	1:10	5/250	non-ionic	0	6
H	55	1:10	5/250	amphoteric	0	6
I	55	1:10	5/250	cationic	0	6
J	55	1:10	5/250	anionic	0	6
K	55	1:10	5/250	non-ionic	0	8
L	55	1:10	5/250	non-ionic	1	8
M	55	1:10	5/250	non-ionic	0.1	8
N	55	1:10	5/250	non-ionic	0.01	8
O	45	1:10	5/250	non-ionic	0.01	8
P	35	1:10	5/250	non-ionic	0.01	8
Q	55	1:10	5/250	non-ionic	0.01	4
R	55	1:10	5/250	non-ionic	0.01	2
S	55	1:10	5/250	non-ionic	0.01	0

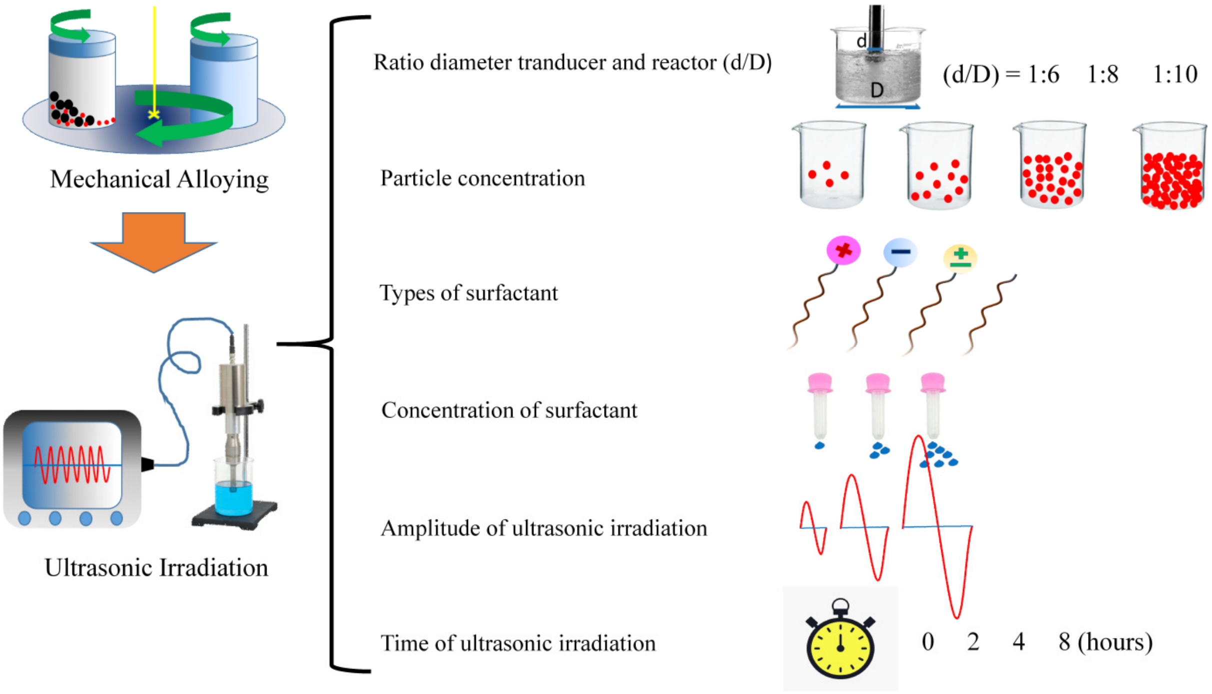

Figure 1. Schematic illustration of the combined destruction process.

X-ray diffraction (XRD, Miniplex 600, Rigaku, Tokyo, Japan) was used to confirm the formation of BHF after sintering and for its structural analysis. The particle size distribution of $BaFe_{11.2}Mg_{0.4}Al_{0.4}O_{19}$ was measured using a particle size analyzer (PSA, Beckman Coulter), and the sample's magnetic properties were characterized using a vibrating sample magnetometer (VSM, OXFORD type 1.2H). The absorption of the reflection loss was observed using a vector network analyzer (VNA, PNA-L N5232A, Keysight). A VNA works by firing electromagnetic waves at a test sample with a thickness of 2 mm at a wavelength of 8.2–12.4 GHz. The VNA characterization results are permeability, permittivity, and parameter S values, which determine the transmission and reflection levels. The reflection loss was computed using the Nicholson–Ross–Weir (NRW) method [25], and the results of the measurement of the transmission signal (S21) and reflection signal (S11) were determined according to Equations (1) and (2).

$$RL\ (dB) = 20\ log \left| \frac{Z-1}{Z+1} \right| \tag{1}$$

$$Z = \sqrt{\frac{\mu}{\varepsilon}}\ tanh\left[\left(-\frac{j2\pi f d}{c} \right) \sqrt{(\mu\varepsilon)} \right] \tag{2}$$

where the characteristic impedance of samples is Z, the complex relative permittivity (ε), the complex relative permeability (μ), the light velocity (c), the frequency of the electromagnetic wave (f), and the thickness of the samples (d) are also calculated. The sample morphology was characterized using Zeiss Scanning Electron Microscopy. The research design for the fixed and free variables is summarized in Table 1.

3. Results and Discussions

3.1. Synthesis of $BaFe_{11.2}Mg_{0.4}Al_{0.4}O_{19}$ through Mechanical Alloying

Figure 2 shows the XRD patterns of the sintered BHF without and with Mg-Al dopants. The single phase of BHF was successfully synthesized using a top-down method, as shown in Figure 2. According to COD#98-006-0986, these patterns were matched and belonged to $BaFe_{12}O_{19}$. Interestingly, Mg-Al doped was synthesized as a single phase without secondary phase

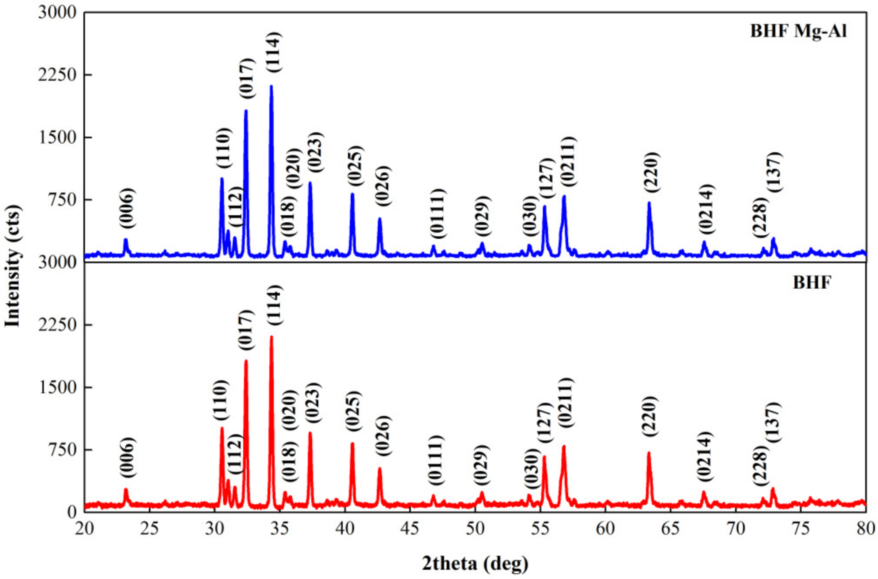

Figure 2. X-ray diffraction pattern of BHF and Mg-Al doped BHF.

Furthermore, using the Rietveld refinement method, we analyzed those patterns and their fitting, which are presented in Figure 3.

Table 2 shows the detailed fitting results. The model data were relatively fitted against the standard data, as indicated by the value of the goodness of fit < 1.2. Indeed, adding Mg-Al decreased the cell volume due to the difference in the ionic radius of Mg-Al and Fe, as shown in Table 2. The shrinkage of lattice parameters a and c occurred due to the substitution process between Fe^{3+} ions with Mg^{2+} and Al^{3+} ions. Magnesium and aluminum have an ionic radius of 0.72 Å and 0.51 Å, respectively, while Fe^{3+} ions have an ionic radius of 0.64 Å [12]. The substitution of a smaller ions size causes a small substitution phenomenon characterized by the shrinkage of the lattice parameters. With a constant mass, the decrease in the value of the lattice parameter causes a decrease in the unit cell volume, thus causing an increase in the density value.

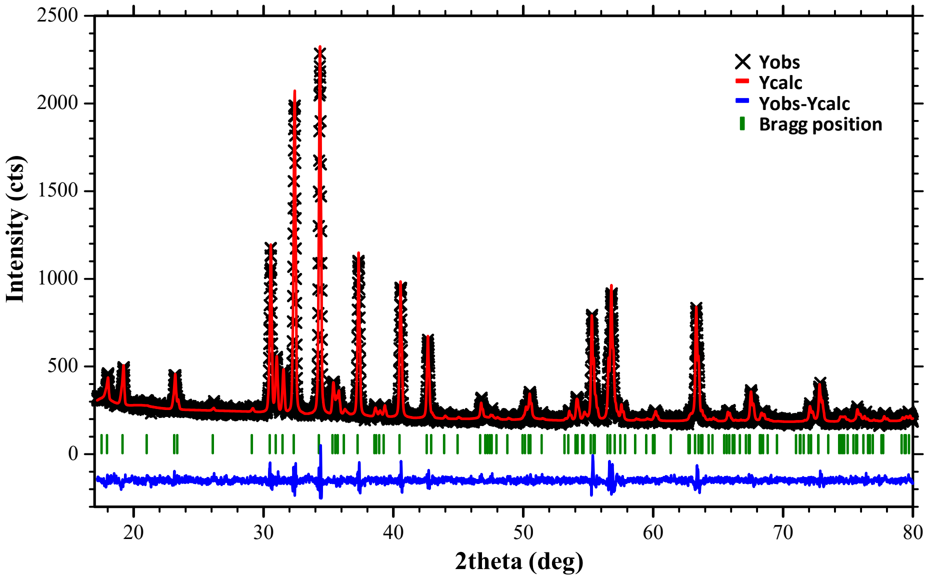

Figure 3. Rietveld analysis of $BaFe_{11.2}Mg_{0.4}Al_{0.4}O_{19}$.

Table 2. Fitting results of BHF and Mg-Al doped BHF.

Description	BHF	Mg-Al Doped BHF
Goodness of fit	1.16	1.26
Chemical formula	$BaFe_{12}O_{19}$	$BaFe_{12}O_{19}$
Calculated density (g/cm^3)	5.29	5.31
Crystal system	Hexagonal	Hexagonal
Space group	P63/mmc	P63/mmc
Crystallite size (Å)	956.2	950.9
Lattice parameters (Å)		
a, b	5.89	5.87
c	23.21	23.19
α, β (deg.)	90	90
γ (deg.)	120	120
Volume of cell (Å^3)	696.52	695.39

3.2. Scanning Electron Microscopy Results

SEM characterization was carried out to determine the morphology of the synthesized material using the combined destruction method. Figure 4 displays the morphology of $BaFe_{11.2}Mg_{0.4}Al_{0.4}O_{19}$ as a result of SEM characterization. At 30,000 times magnification, the material $BaFe_{11.2}Mg_{0.4}Al_{0.4}O_{19}$ had an irregular crystal shape.

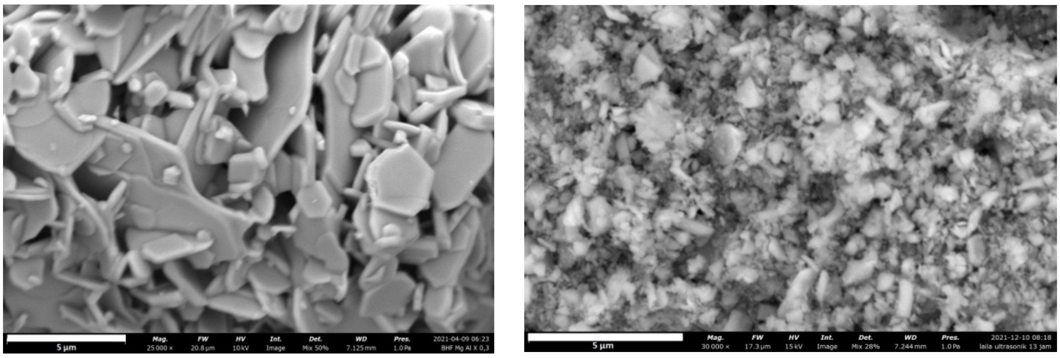

(**a**) (**b**)

Figure 4. Micrograph SEM $BaFe_{11.2}Mg_{0.4}Al_{0.4}O_{19}$: (**a**) re-milling; (**b**) sonication at 8 h.

Based on the XRD characterization shown in Table 2, the Mg-Al ion substitution did not affect the barium hexaferrite's hexagonal crystal structure, which is in accordance with the findings of previous studies [12]. Based on the results of previous researchers, the nanoparticles produced using the top-down method have high aggregation, resulting in a heterogeneous and difficult-to-control morphology and the possibility of crystal defects [26]. The heterogeneous shape of the particles is an advantage, as it can more perfectly reflect electromagnetic waves in all directions. The irregularity of particle morphology is caused by the top-down synthesis method through which a bulk sample is broken down into small particles. The ultrasonic destruction process causes the hexagonal crystal structure to become irregular because high-power ultrasonic waves split the particles. Previous researchers also confirmed this condition on BHF Eu-Nd dopants [20].

3.3. High-Power Ultrasonic Irradiation Process Parameters

High-power ultrasonic irradiation causes cavitation bubbles to form. Cavitation is the process of bursting bubbles in a liquid. The cavitation process is bridged by the presence of the air dissolved in a sonication medium. The air, with the help of ultrasonic irradiation, forms clusters so that larger bubbles are formed and continue to grow. Then, the bubble will burst if it reaches the excess surface tension limit. The bursting of the bubble causes a spontaneous release of energy that produces atomic heat (~5000 K), high pressure (~1000 atm), heating rate (>10^9 K/s), and liquid velocity (~400 km/h) [27,28]. This explosion causes extensive energy propagation in the liquid so that the particles dispersed in this liquid undergo particle destruction, thereby reducing the size of the nanometer particles.

Several process parameters affect the success of ultrasonic irradiation, including the ratio of the transducer diameter to the reactor diameter, the particle density in the reactor, the amplitude, the ultrasonic time, the temperature and pressure in the ultrasonic reactor, and viscosity. Each parameter must be controlled and adjusted to the nature of the material processed. The existence of the type and concentration of surfactants prevents the agglomeration of the resulting nanoparticles. Combining two destruction models via milling and ultrasonic irradiation will significantly reduce particle size.

3.3.1. Effect of d/D Ratio on Particle Size Reduction

The d/D ratio is known to affect the effectiveness of particle size reduction during the ultrasonic irradiation process. The larger the d/D ratio, the more effective it will be to produce the smaller particles [29]. Table 1 shows the analysis of the effects of the d/D ratios of 1:6, 1:8, and 1:10 on the effectiveness of the particle size reduction. Samples A, B, and C in Figure 5 shows the inverse relationship between sedimentation rate and d/D ratio.

Figure 6 presents the narrowing results of the particle size distribution as the d/D ratio increased, making the sample more homogeneous. The average particle size at a d/D ratio of 1:6 was 619 nm. At the ratio of 1:8, the particle size was 561 nm (reduced by 9.4%), and the particle size at a ratio of 1:10 was 270 nm (reduced by 52%). Ultrasonic irradiation is most effective in reducing particle size at a d/D ratio of 1:10. The larger the surface area of the reactor, the more the particles will spread over the entire surface so that the particles do not accumulate and cover the path of the bubble cavity formation. When the particle density increase, the initiation of bubble cavity formation is limited, so the particle size reduction is not maximal.

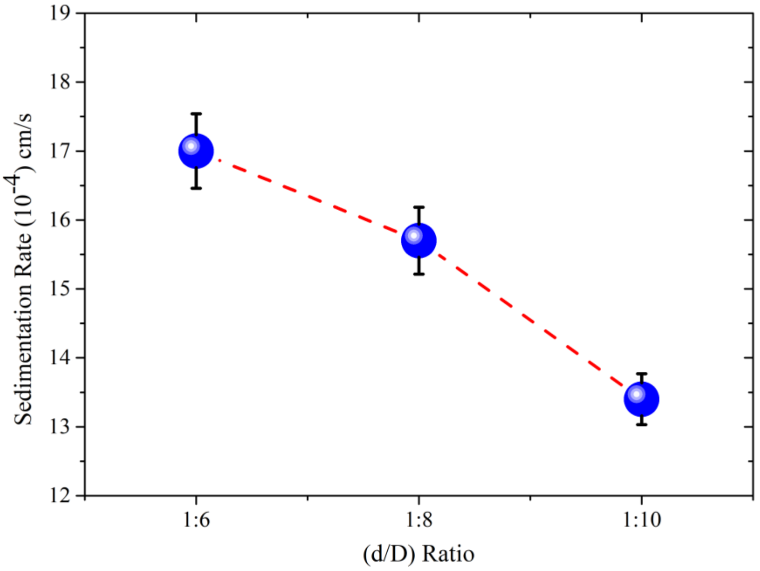

Figure 5. Effect of d/D ratio on sedimentation rate of $BaFe_{11.2}Mg_{0.4}Al_{0.4}O_{19}$.

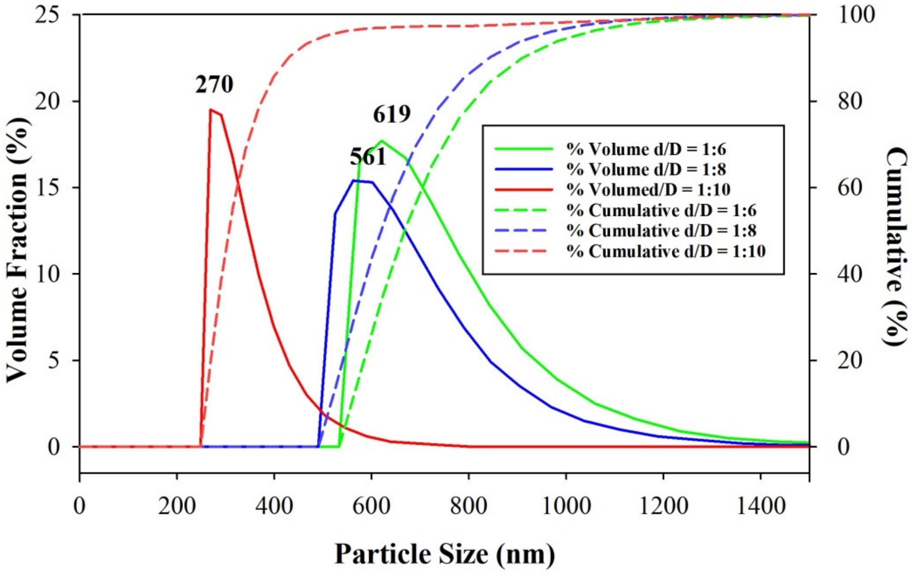

Figure 6. Effect of d/D ratio on the particle size distribution.

3.3.2. Effect of Sonication Process Particle Density on Particle Size Reduction

The results of samples C, D, E, and F listed in Table 1 are presented in Figures 7 and 8. Particle density affects the effectiveness of particle size reduction during ultrasonic irradiation. The decrease in particle density is directly proportional to the decrease in particle size [30]. Figure 7 shows that the particle density was directly proportional to the deposition rate.

The sample with the lowest particle density produced a solution with the lowest settling velocity with a narrow particle size distribution so that the particles were more homogeneous. Figure 8 shows the decrease in the particle density on ultrasonic irradiation, effectively reducing the particle size up to 24.4%.

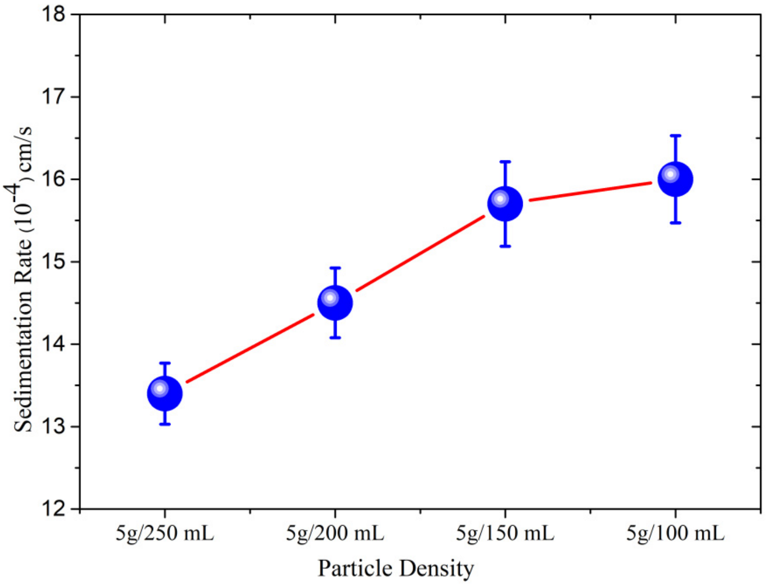

Figure 7. Effect of particle density on sedimentation rate of $BaFe_{11.2}Mg_{0.4}Al_{0.4}O_{19}$.

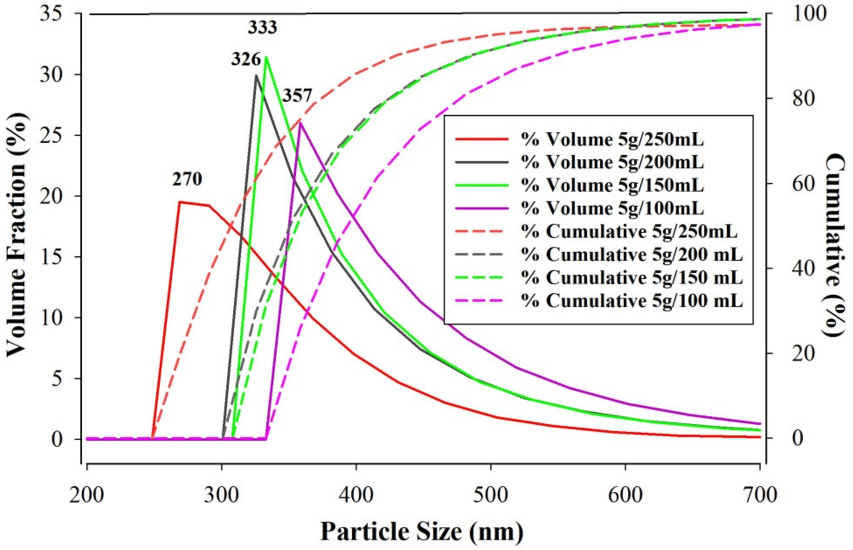

Figure 8. Effect of particle density on the particle size distribution of $BaFe_{11.2}Mg_{0.4}Al_{0.4}O_{19}$.

3.3.3. Effect of Surfactant Type in Preventing Agglomeration

Barium hexaferrite is a magnetic material. When the particles are reduced, they have a high chance of agglomeration. Surfactants are surface-active agents that play influential roles in preventing the agglomeration of nanoparticles. Based on the results of samples C, G, H, I, and J listed in Table 1, the use of surfactants affected the particle size and its distribution, as shown in Figure 9. Without the surfactants, the samples had an average particle size of 270 nm. The amphoteric surfactant is a type of surfactant that has an alkyl part with a positive and negative charge. The addition of an amphoteric surfactant almost did not significantly change when considering the 267 nm particle size. The anionic and cationic surfactants decreased the average particle size by 215 nm and 191 nm, respectively. Meanwhile, the non-ionic surfactants with no charge were the most effective in reducing the particle size by up to 142 nm.

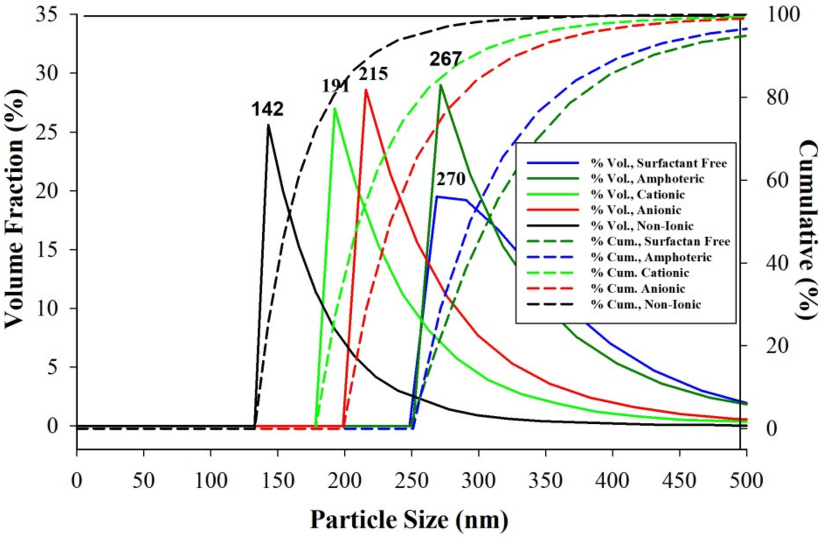

Figure 9. Effect of surfactant type on particle size distribution of $BaFe_{11.2}Mg_{0.4}Al_{0.4}O_{19}$.

3.3.4. Effect of Surfactant Concentration on Preventing Agglomeration

An appropriate amount of surfactant is effective in preventing the agglomeration of nanoparticles. Figure 9 shows that the selected surfactant was non-ionic, a surfactant that did not contain cations and anions. As shown in Table 1, samples K, L, M, and N were analyzed for the effectiveness of the non-ionic surfactant at concentrations of 0%, 1%, 0.1%, and 0.01%, the results of which are shown in Figure 10. Using the non-ionic surfactant of 0.01% was most effective in preventing agglomeration, resulting in the slightest mean particle size of 21 nm with a deviation of 3.9.

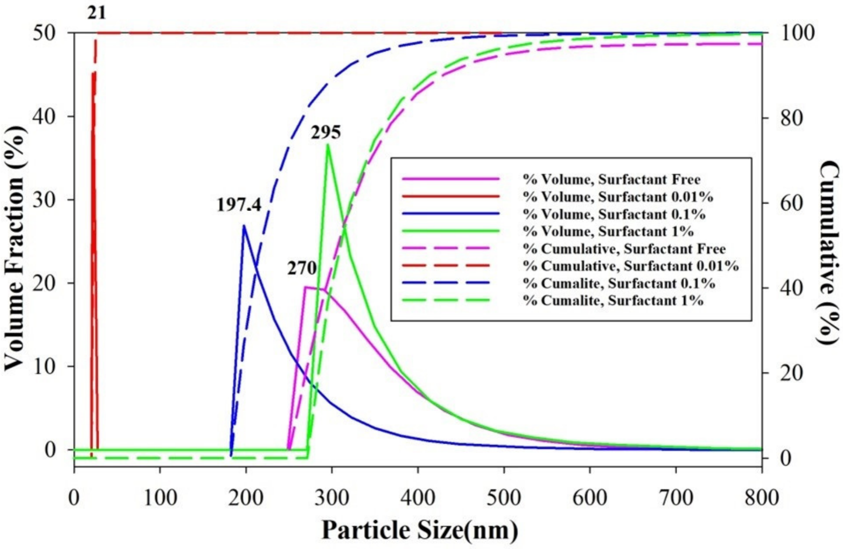

Figure 10. Effect of surfactant concentration on particle size distribution of $BaFe_{11.2}Mg_{0.4}Al_{0.4}O_{19}$.

In general, the smallest particles are unstable due to their high electrostatic forces. The smallest ultrasonic-crushed particles must mix with a surfactant as a surface-active agent. The right type and concentration of a surfactant are needed to prevent agglomeration. The non-ionic surfactant of 0.01% and $BaFe_{11.2}Mg_{0.4}Al_{0.4}O_{19}$ nanoparticles size 21 nm successfully interacted to form a sol.

The non-ionic surfactant surrounded and protected $BaFe_{11.2}Mg_{0.4}Al_{0.4}O_{19}$ particles from the interactions between the particles through Coulomb repulsion between the surfaces of $BaFe_{11.2}Mg_{0.4}Al_{0.4}O_{19}$ particles, as shown in Figure 11.

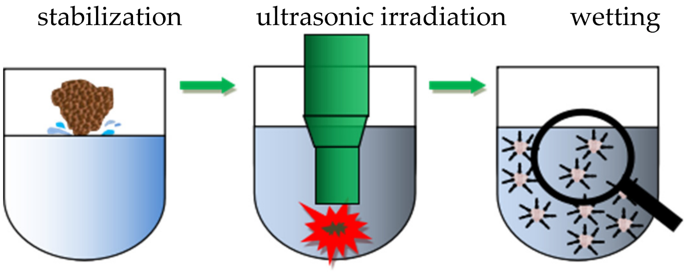

Figure 11. Particle stabilization mechanism.

Based on previous research, the use of surfactants with low concentrations was successful in preventing agglomeration. Excessive surfactant concentrations causes critical micelle concentration (CMC). The excessive use of surfactants tends to increase the likelihood of individual stable particles recombining to form clusters [31].

3.3.5. Effect of Amplitude on The Effectiveness of Particle Size Reduction

The amplitude of the ultrasonic destruction process describes the intensity of the acceleration to produce cavitation bubble. As shown in Table 1, samples N, O, and P were analyzed via ultrasonic irradiation with amplitude variations of 35%, 45%, and 55%. Figure 12 shows that increasing the amplitude decreased the average particle size. Using a 55% amplitude for sonication resulted in the lowest particle size reduction of 21 nm.

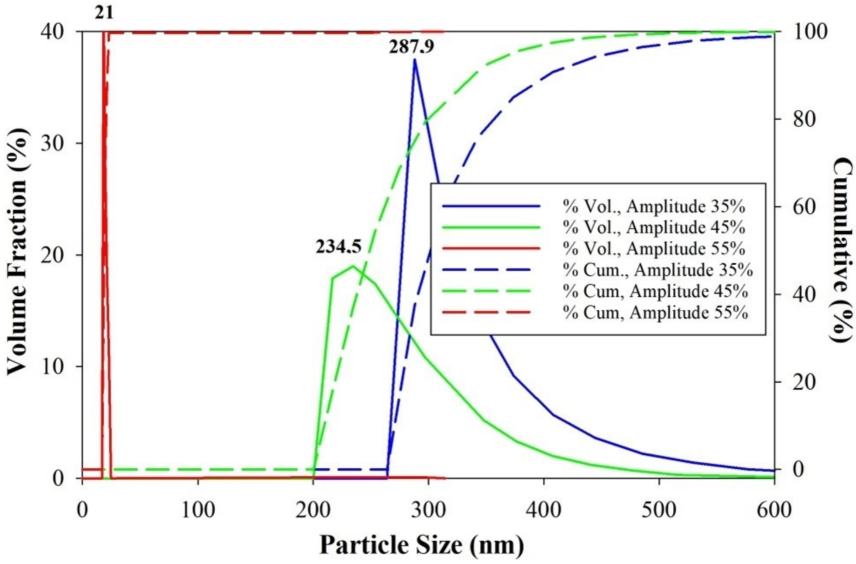

Figure 12. Effect of amplitude on particle size distribution of $BaFe_{11.2}Mg_{0.4}Al_{0.4}O_{19}$.

Transducer and amplitude have a linear relationship in producing cavitation bubbles with different effects. As the transducer power increased, the cavitation bubbles were more intensively crushed along with the BHF sample [32,33]. Equation (3) is used to calculate the probe power required for the transducer to vibrate an ultrasonic wave [34], which shows that the dissipation energy ($P_{dissipation}$) is proportional to A^2.

$$P_{dissipation} = \frac{1}{2} A^2 \, (2 \, f \, \pi) \, ^2 S \, Z \, (Watt) \tag{3}$$

where Z = acoustic impedance in water, S = probe surface area (m^2), f = frequency (Hz), and A = amplitude (m). As shown in Equation (4), the power (E) is required for the transducer to vibrate the wave.

$$E = \frac{1}{2}\,k\,A^2\,(Joule) \;\rightarrow\; P = \frac{1}{2}\,ktA^2\,(Watt) \tag{4}$$

where k = constant (N/m), and the relationship between the power and the amplitude squared is linear, i.e., $P{\sim}A^2$, which shows that the amplitude plays a significant role in reducing the particle size. The larger the amplitude, the more the number of cavitation bubbles that are formed and the greater the dissipation energy generated to break the $BaFe_{11.2}Mg_{0.4}Al_{0.4}O_{19}$ particles into nanometer size.

3.3.6. Effect of Sonication Time on Particle Size Reduction

The absorption of EM waves in the absorber material can be increased by reducing the particle size. The smaller particle size causes the higher absorption of electromagnetic waves with a wider absorption range. As shown in Table 1, samples S, R, Q, and N were studied with variations in the sonication time of 0, 2, 4, and 8 h, the results of which are shown in Figure 13. A successive increase in the ultrasonic irradiation time (0, 2, 4, and 8) h resulted in a very significant reduction in the particle size (373.3, 249.7, 195.2, and 21 nm). The increase in the ultrasonic irradiation time of 8 h resulted in the smallest particle size and more homogeneous particles with a narrow size distribution. The increase in the ultrasonic irradiation time allowed the particles to continue to be fragmented into smaller ones, in agreement with the findings of previous studies [30]. In previous studies mechanical alloying followed by ultrasonic irradiation revealed that Mn-Ti doped BHF had a particle size of 95 nm after 12 h of sonication [4]. The advantage of this study is that the 8 h sonication time effectively reduces particle size to 21 nm. This shorter nanoparticle synthesis time proves the importance of properly controlling the sonication process parameters. Increasing the sonication time does not always result in finer particle size [19].

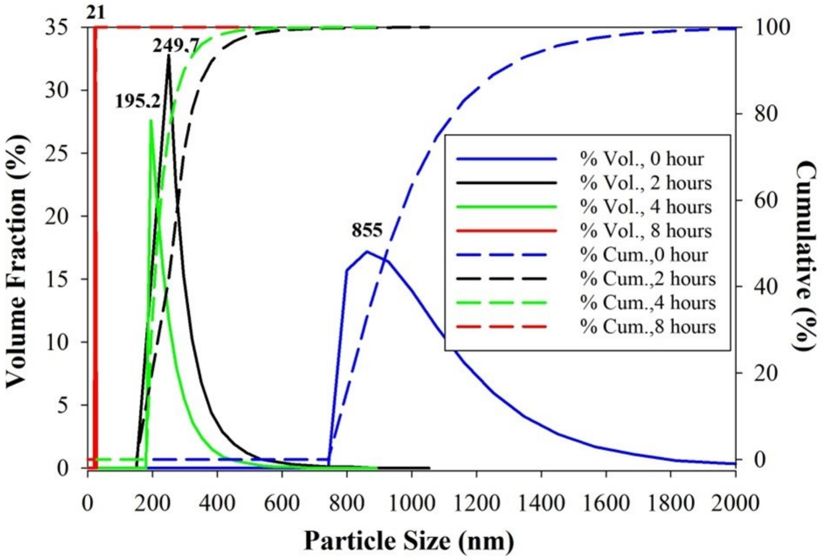

Figure 13. Effect of sonication time on particle size distribution of $BaFe_{11.2}Mg_{0.4}Al_{0.4}O_{19}$.

3.4. *Analysis of Vector Network Analyzer*

The vector network analyzer characterization was carried out to determine the reflection loss. The $BaFe_{11.2}Mg_{0.4}Al_{0.4}O_{19}$ nanometer samples were expected to have the lowest RL with the maximum absorption. Figure 14a shows that the d/D ratio at 1:10 produced $BaFe_{11.2}Mg_{0.4}Al_{0.4}O_{19}$ measuring 270 nm with an RL of −12.9232 dB (94.99% absorption).

Figure 14b shows the lowest particle density variation of 5 g/250 mL resulting in an RL of −12.9232 dB (94.99% absorption). Figure 14c shows that the non-ionic surfactants effectively reduced the particle size of $BaFe_{11.2}Mg_{0.4}Al_{0.4}O_{19}$ to 142 nm, resulting in a reflection loss of −19.0789 dB (98.74%). The decrease in the reflection loss was generally affected by a reduction in particle size.

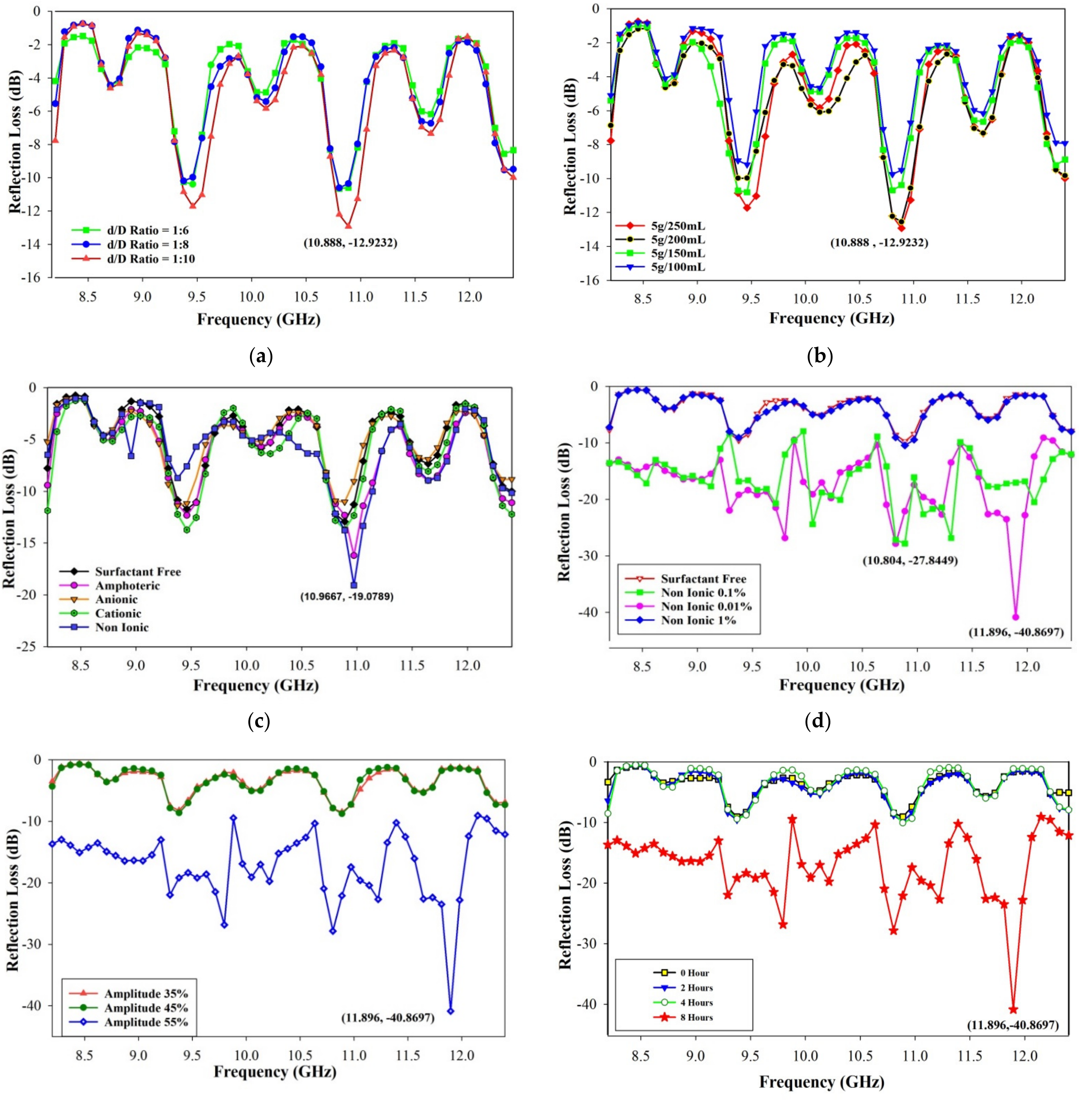

(**a**) (**b**)

(**c**) (**d**)

(**e**) (**f**)

Figure 14. Reflection loss of $BaFe_{11.2}Mg_{0.4}Al_{0.4}O_{19}$ toward (**a**) d/D ratio, (**b**) particle density, (**c**) surfactant type, (**d**) surfactant concentration, (**e**) amplitude, and (**f**) sonication time.

Figure 14d shows the reflection loss curve for variations in surfactant concentration. The ultrasonic irradiation process without surfactant and adding 1% surfactant showed an absorption trend equal to RL −10.43 dB at 10.888 GHz (90% absorption). The surfactant concentration of 0.1% resulted in a lower RL of −27.8449 dB at 10.804 GHz (99.84%). The surfactant concentration of 0.01% resulted in the lowest RL −40.8697 dB at 11.896 GHz (maximum absorption of 99.99%). The top-down method in this study is more eco-friendly, free of waste with maximum absorption of the electromagnetic waves. This study showed that microwave absorption Mg-Al doped BHF significantly improved than Mn-Ti doped BHF, with RL of −19.75 dB at 13.6 GHz (90% absorption) [4]. The reflection loss for the amplitude variation shows in Figure 14e. Ultrasonic irradiation with 35% and 45% amplitude showed the same absorption trend with RL close to −10 dB (absorption < 90%). In comparison, the 55% amplitude variation produced the lowest RL of up to −40.8697 dB at 11.896 GHz frequency. The reduction in particle size is directly proportional to the square of the amplitude, according to Equations (3) and (4). Increasing the amplitude effectively reduced the particle size so that the reflected electromagnetic waves could be canceled. Figure 14f shows the curve of the effect of the sonication time on the reflection loss. The ultrasonic destruction from 0 to 4 h showed the same absorption trend of RL −10 dB. The sonication of $BaFe_{11.2}Mg_{0.4}Al_{0.4}O_{19}$ for 8 h resulted in the smallest average particle size of 21 nm with the lowest RL of −40.8697 dB, and 99.99% absorption at 11.896 GHz. Many factors contributed to a reduced particle size of barium hexaferrite as a radar-absorbing material, so it enhanced the absorption of electromagnetic waves, increasing it from 90% [4] found in a previous study to 99.99% in this study. The element substituted for barium hexaferrite had a significant impact. Previous studies used Mn-Ti, while this study used Mg-Al. The technical parameters of sonication can be controlled very well at present. This study proved that the shorter sonication time of 8 h effectively reduced the particle size to 21 nm with a reflection loss of −40.8697 dB (99.99%). In the previous study, 12 h of sonication were only able to reduce the particle size to 95 nm, with a reflection loss of −19.75 dB (90%). Significant changes in decreasing the RL and increasing the absorption of electromagnetic waves indicated success in controlling the sonication parameters. Sonication with optimal parameters effectively results in particle size reduction. Smaller particles increase the interface's polarization and the absorption of electromagnetic waves [35,36].

3.5. Magnetic Properties of Mg-Al-Doped Barium Hexaferrite

The VSM characterization produced a magnetic hysteresis curve (M–H) to analyze the effect of Mg-Al substitution on the magnetic properties of barium hexaferrite. The hysteresis loop, coercivity, saturation, and remanence magnetization of BHF doped with Mg-Al are shown in Figure 15. The substitution resulted in interactions between domains, and the type of coordination in BHF changed because the Mg-Al ion radius was different from the Fe ion radius. The material of $BaFe_{11.2}Mg_{0.4}Al_{0.4}O_{19}$ was synthesized using mechanical alloying and ultrasonic irradiation methods. In BHF doped with Mg-Al, the magnetic remanence (Mr) decreased from 29.28 emu/g to 18.50 emu/g, and the coercivity reduced from 0.12 T to 0.08 T. The Mg-Al dopants changed BHF from a hard magnetic material into a soft magnetic one. This manifested in its decreased coercivity and magnetic remanence and narrowed hysteresis loop [6,11,37].

Figure 15 shows that Mg-Al-doped BHF slightly increased the saturation magnetization. This effect can be evaluated by analyzing the effect of Mg-Al substitution on the crystal structure of BHF, as shown in Figure 16.

It is well-known that there are five different sites in the unit cell of $BaFe_{12}O_{19}$ in which Fe^{3+} ions are distributed on five Wyckoff positions, namely 12k, 4f2, 4f1, 2b, and 2a, which are based on its coordination with O^{2-} ions. These five Wyckoff positions are grouped as three octahedral sites (12k, 4f2, 2a), one tetrahedral site (4f1), and one bipyramidal site (2b) with the abundances of 6, 2, 1, 2, and 1, respectively [38]. Table 3 show the ionic radi for Fe^{3+}, Mg^{2+} and Al^{3+} as a function on their complex coordination with oxygen, which can be use to identify the partial substitution of Fe^{3+} ion inside the $BaFe_{12}O_{19}$ crystal structure. The magnetic spins of Fe^{3+} ions are arranged upward at 12k, 2b, and 2a and downward at 4f1 and 4f2 sites. Therefore, the net magnetization originates from Fe^{3+} ions with upward spins. The substitution of the Fe^{3+} ions may result in different variations in the magnetic properties of the substituted Ba hexaferrite.

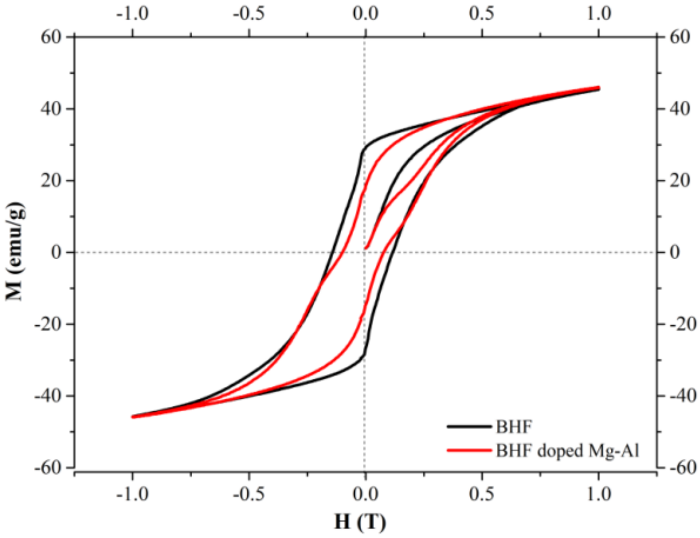

Figure 15. The hysteresis loop of BHF and Mg-Al doped BHF.

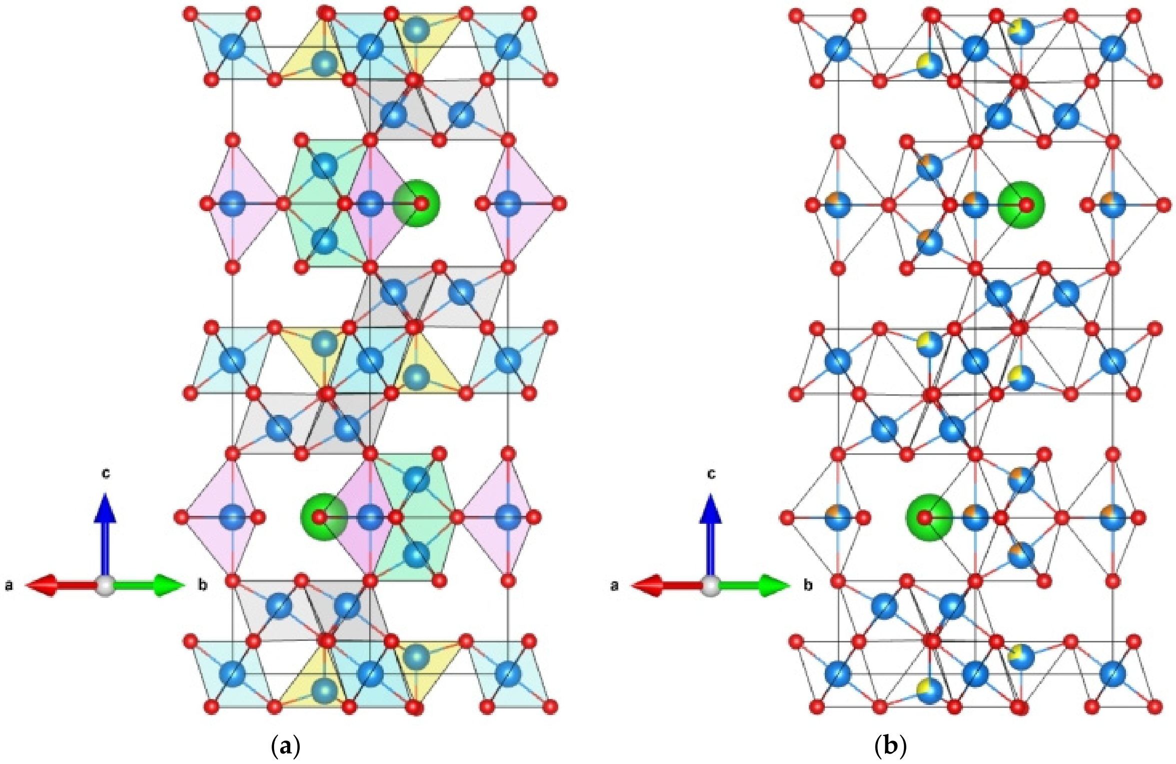

(**a**) (**b**)

Figure 16. Crystal structure of (**a**) $BaFe_{12}O_{19}$ with the five different Fe^{3+} sites and (**b**) $BaFe_{11.2}Mg_{0.4}Al_{0.4}O_{19}$ with most likely site occupancy. Polyhedral color code: grey, 12k; green, 4f2; blue, 2a; yellow, 4f1; pink, 2b; atomic color code: green, Ba; red, O; navy, Fe; orange, Mg; yellow, Al.

Table 3. Crystal radius of Fe^{3+}, Mg^{2+}, and Al^{3+} as a function of coordination complex [39] *.

Ionic	Electronegativity	Ionic Radius (Å)		
		IV (Tetrahedral)	V (Trigonal)	VII (Octahedral)
Fe^{3+}	1.83	0.49	0.58	0.65
Mg^{2+}	1.31	0.57	0.66	0.72
Al^{3+}	1.61	0.39	0.48	0.353

* Reproduced with permission of the International Union of Crystallography.

The polyhedral volumes of Fe^{3+} ion in $BaFe_{12}O_{19}$ crystal structure after Rietveld refinement are 10.1505 Å^3, 7.2462 Å^3, and 3.6346 Å^3 namely octahedral, trigonal, and tetrahedral, respectively. Based on the ionic radii in Table 3, the octahedral substitution site is more likely to be occupied by Mg^{2+}, and the tetrahedral site is more likely to be occupied by Al^{3+}, while both can occupy the trigonal site. This hypothesis can be validated using the VSM result, where the increase in magnetic saturation (M_s) is evidence that Mg^{2+} partially occupies the downward octahedral site (4f2), and Al^{3+} partially occupies the downward tetrahedral site (4f1). The significant decrease in coercivity (H_c) is evidence of the partial substitution of Fe^{3+} ions upward in the bipyramidal site (2b), which gives the most values of the anisotropy constant (K_1) [40]. It also decreases the upward spin due to the non-magnetic ion substitution as a consequence of a slight increase in M_s.

4. Conclusions

$BaFe_{11.2}Mg_{0.4}Al_{0.4}O_{19}$ nanoparticles were successfully synthesized using mechanical alloying and high-power ultrasonic irradiation methods. The d/D ratio of 1:10 and particle density of 5 g/250 mL effectively reduced the particle size of $BaFe_{11.2}Mg_{0.4}Al_{0.4}O_{19}$ up to 270 nm. The most effective non-ionic surfactants prevented agglomeration and reduced the particle size to 142 nm with a reflection loss of −19.0789 dB and an absorption of 98.74%. The reduction in the particle size was directly proportional to the decrease in the reflection loss. An ultrasonic irradiation time of 8 h, with 55% amplitude, and the addition of 0.01% non-ionic surfactant were the best parameters for ultrasonic irradiation to reduce the particle size by up to 21 nm. The minimum reflection loss achieved was −40.8697 dB at 11.896 GHz, which indicates a microwave absorber level of up to 99.99%.

Author Contributions: Conceptualization, E.Y. and A.N.; methodology, E.Y.; software, M.M.; validation, M.A.R.S. and L.C.C.; formal analysis, L.C.C.; investigation, M.R.; data curation, E.Y.; writing—original draft preparation, E.Y.; writing—review and editing, E.Y. and M.M. All authors have read and agreed to the published version of the manuscript.

Funding: This work was financially supported by the Ministry of Education, Culture, Research, and Technology Republic of Indonesia under the scheme of Penelitian Dasar Kompetitif Nasional grant No.144/E5/PG.02.00.PT/2022.

Institutional Review Board Statement: Not applicable.

Informed Consent Statement: Not applicable.

Data Availability Statement: Not applicable.

Acknowledgments: All authors are grateful to the Radar Cross Section Laboratory, the Ministry of Defense, the Republic of Indonesia, and the permission to use the VNA characterization facility for absorber material testing.

Conflicts of Interest: The authors declare no conflict of interest.

References

1. Al-Mattarneh, H. Development and characterization of microwave absorber composite material. *Int. J. Eng. Technol.* **2018**, *7*, 54–58. [CrossRef]
2. Handoko, E.; Budi, S.; Sugihartono, I.; Marpaung, M.A.; Jalil, Z.; Taufiq, A.; Alaydrus, M. Microwave absorption performance of barium hexaferrite multi-nanolayers. *Mater. Express* **2020**, *10*, 1328–1336. [CrossRef]
3. Gultom, G.; Rianna, M.; Sebayang, P.; Ginting, M. The effect of Mg-Al binary doped barium hexaferrite for enhanced microwave absorption performance. *Case Stud. Therm. Eng.* **2020**, *18*, 100580. [CrossRef]
4. Yustanti, E.; Trenggono, A.; Manaf, A. Physical and Microwave Absorption Characteristics of High Powered. *Int. J. Technol.* **2020**, *11*, 310–321. [CrossRef]
5. Rianna, M.; Sembiring, T.; Kurniawan, C.; Setiadi, E.A.; Simbolon, S.; Ginting, M.; Sebayang, P. Microstructure and magnetic properties of $BaFe_{12-2x}Mg_xAl_xO_{19}$ for microwave absorbing materials. *Int. J. Appl. Eng. Res.* **2017**, *12*, 6586–6590.
6. Soman, V.V.; Nanoti, V.M.; Kulkarni, D.K. Dielectric and magnetic properties of Mg–Ti substituted barium hexaferrite. *Ceram. Int.* **2013**, *39*, 5713–5723. [CrossRef]
7. Seyyed Afghahi, S.S.; Jafarian, M.; Salehi, M.; Atassi, Y. Improvement of the performance of microwave X band absorbers based on pure and doped Ba-hexaferrite. *J. Magn. Magn. Mater.* **2017**, *421*, 340–348. [CrossRef]
8. Singh, J.; Singh, C.; Bai, Y.; Kaur, D.; Bindra Narang, S.; James Raju, K.C.; Dhruv, P.N.; Jotania, R.; Joseph, A.; Joshi, R. Role of phase, grain morphology and impedance properties in tailoring of Barium Strontium hexaferrites for microwave absorber/attenuator applications. *Mater. Sci. Eng. B Solid-State Mater. Adv. Technol.* **2022**, *281*, 115679. [CrossRef]
9. Hu, F.; Nan, H.; Wang, M.; Lin, Y.; Yang, H.; Qiu, Y.; Wen, B. Construction of core-shell $BaFe_{12}O_{19}$@MnO_2 composite for effectively enhancing microwave absorption performance. *Ceram. Int.* **2021**, *47*, 16579–16587. [CrossRef]
10. Lin, Y.; Liu, Y.; Dai, J.; Wang, L.; Yang, H. Synthesis and microwave absorption properties of plate-like $BaFe_{12}O_{19}$@Fe_3O_4 core-shell composite. *J. Alloys Compd.* **2018**, *739*, 202–210. [CrossRef]
11. Nikmanesh, H.; Moradi, M.; Bordbar, G.H.; Shams Alam, R. Effect of multi dopant barium hexaferrite nanoparticles on the structural, magnetic, and X-Ku bands microwave absorption properties. *J. Alloys Compd.* **2017**, *708*, 99–107. [CrossRef]
12. Rianna, M.; Situmorang, M.; Kurniawan, C.; Tetuko, A.P.; Setiadi, E.A.; Ginting, M.; Sebayang, P. The effect of Mg-Al additive composition on microstructure, magnetic properties, and microwave absorption on $BaFe_{12-2x}Mg_xAl_xO_{19}$ ($x = 0$–0.5) material synthesized from natural iron sand. *Mater. Lett.* **2019**, *256*, 126612. [CrossRef]
13. Kagdi, A.R.; Solanki, N.P.; Carvalho, F.E.; Meena, S.S.; Bhatt, P.; Pullar, R.C.; Jotania, R.B. Influence of Mg substitution on structural, magnetic and dielectric properties of X-type barium–zinc hexaferrites $Ba_2Zn_{2-x}Mg_xFe_{28}O_{46}$. *J. Alloys Compd.* **2018**, *741*, 377–391. [CrossRef]
14. Chen, Z.; Mu, D.; Liu, T.; He, Z.; Zhang, Y.; Yang, H.; Ouyang, J. PANI/$BaFe_{12}O_{19}$@Halloysite ternary composites as novel microwave absorbent. *J. Colloid Interface Sci.* **2021**, *582*, 137–148. [CrossRef] [PubMed]
15. Chokprasombat, K.; Lohmaah, A.; Pinitsoontorn, S.; Sirisathitkul, C. Effects of bismuth and bismuth-copper substitutions on structure, morphology, and magnetic properties of sol-gel derived barium hexaferrites. *J. King Saud Univ.-Sci.* **2022**, *34*, 101682. [CrossRef]
16. Nag, A.; Bose, R.S.C.; Venu, K.S.; Singh, H. Influence of particle size on magnetic and electromagnetic properties of hexaferrite synthesised by sol-gel auto combustion route. *Ceram. Int.* **2022**, *48*, 15303–15313. [CrossRef]
17. Suthar, M.; Roy, P.K. Structural, electromagnetic, and Ku-band absorption characterization of La-Mg substituted Y-type barium hexaferrite for EMI shielding application. *Mater. Sci. Eng. B Solid-State Mater. Adv. Technol.* **2022**, *283*, 115801. [CrossRef]
18. Rostami, M.; Jafarpour, M.; Majles Ara, M.H. An investigation on the microwave absorption properties of Co–Al–Ti substituted barium hexaferrite-MWCNT nanocomposites. *J. Alloys Compd.* **2021**, *872*, 159656. [CrossRef]
19. Mahdiani, M.; Soofivand, F.; Salavati-Niasari, M. Investigation of experimental and instrumental parameters on properties of $PbFe_{12}O_{19}$ nanostructures prepared by sonochemical method. *Ultrason. Sonochem.* **2018**, *40*, 271–281. [CrossRef]
20. Almessiere, M.A.; Slimani, Y.; Demir Korkmaz, A.; Baykal, A.; Albetran, H.; Saleh, T.A.; Sertkol, M.; Ercan, I. A study on the spectral, microstructural, and magnetic properties of Eu–Nd double-substituted $Ba_{0.5}Sr_{0.5}Fe_{12}O_{19}$ hexaferrites synthesized by an ultrasonic-assisted approach. *Ultrason. Sonochem.* **2020**, *62*, 104847. [CrossRef]
21. Almessiere, M.A.; Slimani, Y.; Guner, S.; Aldakhil, S.; Korkmaz, A.D.; Sertkol, M.; Gungunes, H.; Yasin, G.; Baykal, A. Ultrasonic synthesis, magnetic and optical characterization of Tm^{3+} and Tb^{3+} ions co-doped barium nanohexaferrites. *J. Solid State Chem.* **2020**, *286*, 121310. [CrossRef]
22. Georgieva, B.; Kolev, S.; Krezhov, K.; Ghelev, C.; Kovacheva, D.; Vertruyen, B.; Closset, R.; Tran, L.M.; Babij, M.; Zaleski, A.J.; et al. Structural and magnetic characterization of Y-type hexaferrite powders prepared by sol-gel auto-combustion and sonochemistry. *J. Magn. Magn. Mater.* **2019**, *477*, 131–135. [CrossRef]
23. Houbi, A.; Aldashevich, Z.A.; Atassi, Y.; Bagasharova Telmanovna, Z.; Saule, M.; Kubanych, K. Microwave absorbing properties of ferrites and their composites: A review. *J. Magn. Magn. Mater.* **2021**, *529*, 167839. [CrossRef]
24. Ji, R.; Yang, M.; Lv, J.; Wang, Z.; Shi, Y.; Song, X.; Xie, A.; Liu, J.; Zhang, M. Carboxylation-induced polyaniline morphology on surfaces of barium hexaferrite nano particles with enhanced microwave absorbing properties. *J. Alloys Compd.* **2021**, *883*, 160839. [CrossRef]
25. Nicolson, A.M.; Ross, G. Measurement of the Intrinsic Properties of Materials by Time-Domain Techniques. *IEEE Trans. Instrum. Meas.* **1970**, *19*, 377–382. [CrossRef]

26. Hessien, M.M.; Radwan, M.; Rashad, M.M. Enhancement of magnetic properties for the barium hexaferrite prepared through ceramic route. *J. Anal. Appl. Pyrolysis* **2007**, *78*, 282–287. [CrossRef]
27. Suslick, K.S. Sonochemistry. In *Comprehensive Coordination Chemistry II*; Elsevier Ltd.: Amsterdam, The Netherlands, 2003; Volume 1, pp. 731–739, ISBN 9780080437484.
28. Suslick, K.S.; Price, G.J. Applications Of Ultrasound To Materials Chemistry. *Annu. Rev. Mater. Sci.* **1999**, *29*, 295–326. [CrossRef]
29. Manaf, A.; Fahmi, A.A.; Yustanti, E. The effect of diameter ratio between transducers and reactor in sonication-assisted synthesis of $Ba_{0.7}Sr_{0.3}TiO_3$ and $Ba_{0.3}Sr_{0.7}TiO_3$ nanoparticles. In Proceedings of the International Symposium on Current Progress in Mathematics and Sciences 2015 (ISCPMS 2015), Depok, Indonesia, 3–4 November 2015; Mart, T., Triyono, D., Eds.; AIP Publishing: Depok, Indonesia, 2016; Volume 1729, pp. 020038-1–020038-4.
30. Yustanti, E.; Hafizah, M.A.E.; Manaf, A. Exploring the Effect of Particle Concentration and Irradiation Time in the Synthesis of Barium Strontium Titanate (BST) $Ba_{(1-X)}SrXTiO_3$ (X:0-1) Nanoparticles by High Power Ultrasonic Irradiation. *Int. J. Technol.* **2016**, *7*, 1016–1025. [CrossRef]
31. Yustanti, E.; Hafizah, M.A.E.; Manaf, A. Surfactant-Assisted Synthesis of $Ba_{0.7}Sr_{0.3}TiO_3$ Nanoparticles by Mechanical Alloying and Ultrasonic Irradiation. In Proceedings of the International Conference on Engineering, Science and Nanotechnology 2016 (ICESNANO 2016), Solo, Indonesia, 3–5 August 2016; American Institute of Physics: Solo, Indonesia, 2017; Volume 1788, pp. 030119-1–030119-4.
32. Fitriana, K.N.; Hafizah, M.A.E.; Manaf, A. Synthesis and Magnetic Characterization of Mn-Ti Substituted $SrO.6Fe_{2\text{-}x}Mn_{x/2}Ti_{x/2}O_3$ ($x = 0.0$–1.0) Nanoparticles by Combined Destruction Process. *Int. J. Technol.* **2017**, *4*, 644–650. [CrossRef]
33. Fitriana, K.N.; Hafizah, M.A.E.; Manaf, A. Structural Modification of Strontium Hexaferrite Through Destruction Process and Ionic Substitution. *AIP Conf. Proc.* **2016**, *1725*, 1–6.
34. Ratoarinoro; Contamine, F.; Wilhelm, A.; Berlan, J.; Delmas, H. Power Measurement in Sonochemistry. *Ultrason. Sonochem.* **1995**, *2*, S43–S47. [CrossRef]
35. Duan, Y.; Guan, H. *Microwave Absorbing Materials*; CRC Press: Boca Raton, FL, USA, 2016; ISBN 9789814745109.
36. Kumar, A.; Agarwala, V.; Singh, D. Effect of particle size of $BaFe_{12}O_{19}$ on the microwave absorption Characteristics in X-band. *Prog. Electromagn. Res. M* **2013**, *29*, 223–236. [CrossRef]
37. Inoue, A.; Kong, F. Soft Magnetic Materials. *Encycl. Smart Mater.* **2021**, *5*, 10–23. [CrossRef]
38. Taryana, Y.; Wahyu, Y.; Manaf, A.; Manawan, M.; Adi, W.A. Structural and microwave absorption properties of $BaFe_{(12-2x)}Sn_xZn_xO_{19}$ ($x=0.05$–1.0) ceramic magnets. *Materialia* **2022**, *23*, 101455. [CrossRef]
39. Shanon, R.D. Revised Effective Ionic Radii and Systematic Studies of Interatomie Distances in Halides and Chaleogenides. *Acta Crystallogr.* **1976**, *A32*, 751–767. [CrossRef]
40. Bsoul, I.; Mahmood, S.H.; Lehlooh, A.F. Structural and magnetic properties of $BaFe_{12\text{-}2x}Ti_xRu_xO_{19}$. *J. Alloys Compd.* **2010**, *498*, 157–161. [CrossRef]